Plasmonic mode analysis on asymmetric ITO/Au/ITO hyperbolic metamaterials using prism coupled spectroscopic ellipsometry

Ka Kin LAM, King Wah Gabriel CHAN, Sheung Mei NG, Hon Fai WONG, Lin Feng FEI, Yu Kuai LIU, Kin Hung FUNG, Chi Wah LEUNG, Chee Leung MAK*

Department of Applied Physics, The Hong Kong Polytechnic University, Hong Kong SAR, China

KEYWORDS: ITO/Au/ITO, asymmetric trilayer, plasmonic properties, ellipsometry, refractive index sensor

ABSTRACT: Various trilayers (ITO-Au-ITO) of constant total thickness 43 nm, with different bottom and top ITO film thicknesses, have been prepared by magnetron sputtering. The effects of the relative position of the inserted gold layer on the trilayers' plasmonic properties have been systemically investigated. In order to study their optical reflectance changes caused by the surface plasmon resonance, total internal reflection ellipsometry (TIRE) has been employed. Two reflectance minima, corresponding to the pseudo-Brewster (PB) and bulk plasmon-polariton (BPP) are observed from the reflectance spectra. The impacts of the light incident angles on the behaviors of these modes have been monitored. The measured reflectivity spectra are match well with the simulated reflectivity spectra based on the Fresnel formalism. For the $ITO_t/Au/ITO_b$ =5/3/35 sample, where the Au layer is positioned closest to the sampling liquid, the BPP mode becomes the sharpest (based on the amplitude as well as half width) as compared to other samples, indicating

that the closer ITO_t/Au interface to the sampling liquid, the stronger observable plasmonic resonance effect. Furthermore, it is found that the dip position of this BPP mode is independent to the angle of incident but is sensitive to the refractive index of the sampling liquid. Our results show that the dip position shifts to shorter wavelength with increasing refractive index of the sampling liquid. This means that the trilayer can be acted as a refractive index sensor. By linear regression, the obtained sensing accuracy is up to 552 nm/RIU. This brings the potential application of this trilayer structure as the surface plasmon enhanced refractive index sensor.

INTRODUCTION

Optical multilayer structures are stack of thin films composited of various materials, and the thickness dimensions of each thin film are close to sub-wavelength range of light. These optical multilayer structures, possessing optical anisotropy along both the in- and out-of-plane (stacking direction) permittivities, usually archive unique and extraordinary optical properties serving specific applications such as optical filters[1-2] or electro-optical modulators[3-4] through controlling their optical absorption ranges. These artificially structured materials are further realized as hyperbolic metamaterials[5] (HMM) which show hyperbolic dispersion in k-space and exhibit various novel optical properties when one of the permittivity tensor becomes negative in certain spectral ranges. Such hyperbolic dispersion can practically applied into optical hyperlens[6] based on emission enhancement[7-8] or surface plasmon amplification by stimulated emission of radiation (SPASER).[9] Among various optical multilayer structures[10-14], ITO/Au/ITO (IAI) trilayer is an interesting type with plasmonic tunability ranging from near-infrared to visible range. IAI trilayer structure, a thin Au-spacer layer sandwiching by top and bottom ITO films (ITO_t/Au/ITO_b), is an

important component exhibiting various epsilon-near-zero (ENZ) surface plasmonic properties in near-infrared (NIR) range with wide range tunability.

In previous studies[15], it is shown that the inserted gold spacer improves the crystallinity of the ITO layer deposited on top of the Au spacer (as compared to the bottom layer). The better crystallinity enhances the overall carrier concentration and carrier mobility that will give rise to the improvement of its optical properties. Moreover, the degree of improvement in electrical as well as optical properties will be more significant as the top ITO layer thickness increases. Therefore, the thicknesses of the IAI structure (in particular, the thickness of the top ITO layer) strongly influence the overall performance of the trilayer structures. This is important as this gives an extra tuning ability in the electrical, optical as well as plasmonic properties of the trilayer structures. Further studies[16] reported on using the variation of the IAI trilayer structure's top and bottom thicknesses simultaneously with a constant Au spacer layer thickness to achieve a wide range of plasmonic resonance wavelength (λ_c) tuning ability of symmetric trilayer structure. Other studies also reported the tuning of the plasmonic properties of ITO/metal/ITO trilayer structure based on other modifications, such as changing of the spacer materials[17-18] and variation of the spacer thickness[15]. However, few studies have been reported on the systematic study of the effects of the position of the spacer layer with respect to the two ITO layers (i.e., the ratio of the top vs bottom layer thickness) on their optical and plasmonic properties.

In this study, magnetron sputtering, being a stable and precise thin film deposition technique, was employed to fabricate the ITO/Au/ITO asymmetric sandwich structures with various top and bottom ITO film thicknesses. A series of trilayer samples, with continuously variation between the top and bottom ITO thicknesses while maintaining the total trilayer thickness to be 43 nm, was fabricated. The selected total thickness of 43 nm was based on our previous symmetric trilayer

sample (the $ITO_t/Au/ITO_b$ with 20 nm top- and 20 nm bottom-ITO thicknesses, and 3 nm gold spacer layer[16]) due to the expected resonance wavelength should be located around the NIR range. The structural, optical and plasmonic properties of these asymmetric sandwich structures were measured in order to understand whether the variation of the top/bottom ITO thickness ratio has any effects on the plasmonic properties of the trilayer structure.

EXPERIMENTAL DETAILS

The ITO and Au layers were deposited on Corning glass substrates (Corning Eagle XG AMLCD glass, USA) using a magnetron sputtering system (Denton sputtering system, USA). The sputtering chamber was evacuated to a base pressure of 10^{-7} torr before the deposition process. During the deposition process, the chamber pressure was maintained at an Argon atmosphere of 10^{-3} torr through a constant Argon flow rate of 30 Standard cubic centimeters (SCCM). For the deposition of ITO layers, an 80W direct current (DC) power was applied to a tin-doped indium oxide (In_2O_3/SnO_2 of 90/10 wt%, ITO thereafter) target; while an 80W radio frequency (RF) power was applied to the Au target (purity:99.99%) in order to sputter the Au layers. The glass substrates were maintained at 100ºC throughout the whole sputtering process for better crystallization of Au layer[15] and higher transparency of ITO layer[19].

The structural properties of the trilayers, including crystal structures and film thicknesses of each deposited layers, were studied by X-ray diffractometer (Rigaku Smart Lab) equipped with Cu Kα radiation source (λ= 0.1541 nm). $\theta - 2\theta$ scan and X-ray reflectivity (XRR) were employed to investigate the crystalline properties and estimate the thicknesses of individual layer, respectively. For the prism coupled spectroscopic ellipsometry measurement, the samples were measured using the Kretschmann configuration as shown in Figure 1. A drop of sampling liquid was first dispersed on the black ellipsometer sample stage, then the glass substrate was put inverted on the sample

stage so that the conductive face is in-contact with the sampling liquid. In our measurement, several common laboratory solvents including paraffin oil, glycerin, isopropyl alcohol (IPA) ethanol or deionized water has been used as the sampling liquid. A 45° K9 (BK-7, HengYang Optical) glass prism (n_s=1.51) was put on top of the glass substrate, an immersion BK-7 matching liquid with n=1.5167 (Cargille Laboratory) was dropped as index matching layer to fill the air gap between the prism and substrate. The sample was back-side illuminated such that the light was incident on metal film through the transparent glass substrate to the conductive thin film and sampling liquid as shown in Figure 1. The Spectra of the ellispmetric parameters ψ and Δ were acquired within the wavelength range between 400 nm and 2000 nm with variable incident angles started from 40° to 66° at a 2° angle step. On the basis of the measured data, the complex permittivities for the simulation of ellipsometry parameters were retrieved by self-developed MATLAB code based on Fresnel reflectance theory.

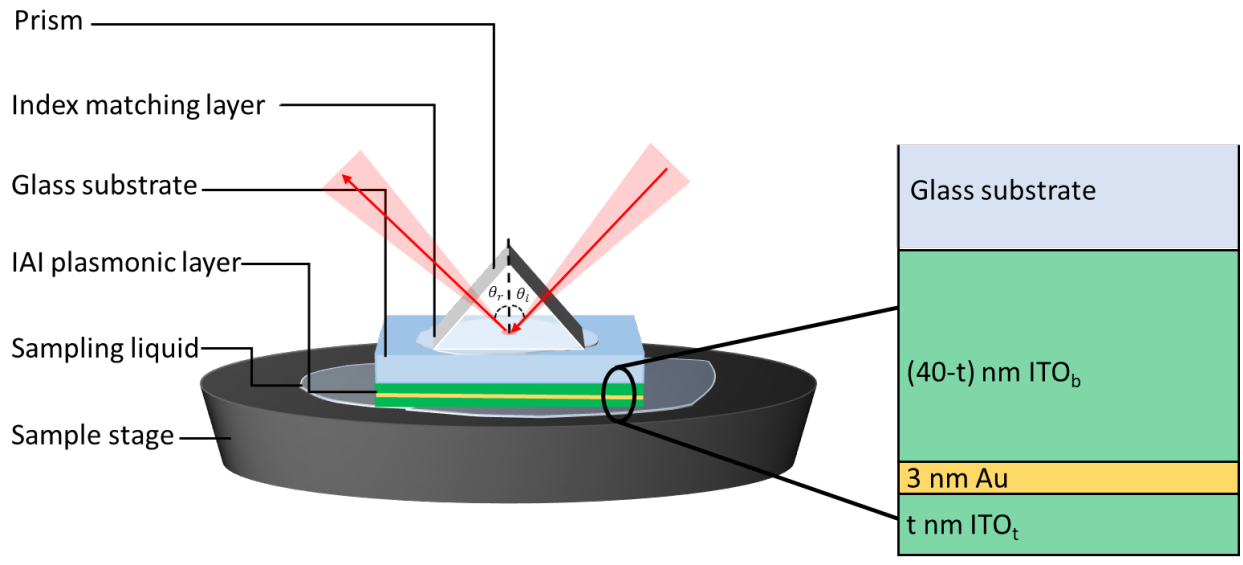

Figure 1 The Kretschmann configuration or Attenuated-Total-Reflection (ATR) configuration, for excitation of plasmon in IAI trilayer structure.

RESULTS AND DISCUSSION

First of all, it is important to confirm whether the trilayer samples exhibit the correct phase with the designated thicknesses by structural characterization. The $\theta - 2\theta$ scan for five asymmetric trilayer samples were reported in last report[16] for demonstrating the top ITO layer possessing better crystallinity than bottom ITO which indicated by smaller the Full Width Half Maximum (FWHM) value in ITO (400) peak as the top ITO layer thickness increase. The full $\theta - 2\theta$ scan of five samples can be referred to the Supporting information.

Then, the thicknesses of each individual layer for all trilayer films were non-destructively characterized by X-Ray Reflectivity (XRR) measurement. Figure 2(a) plots the measured XRR patterns which show high degree of accuracy with the fitted curves. The interlayer thicknesses were extracted through the fitted pattern and the retrieved parameters were consistent with the calibrated deposition condition of magneton sputtering. Also, the ripple pattern, as known as the Kiessig fringes resulting from the interference of reflected X-ray from the film and substrate surfaces[20], continuously spread from 0^o to 6^o and does not decay quickly. This indicates that the deposited trilayer's interfaces possess very low surface roughness. Figure 2(b) inserted the TEM cross-section micrographs. In the micrographs, it is observed that the interfaces of the asymmetric samples are uniform and smooth with no interfacial diffusion. The thickness of the individual layer of the trilayer structure can be confirmed with the assistance of the scale bar, and the measured thicknesses match well with the XRR fitted thicknesses. Therefore, it is believed that the individual layer thicknesses can be controlled precisely by simply control the deposition time.

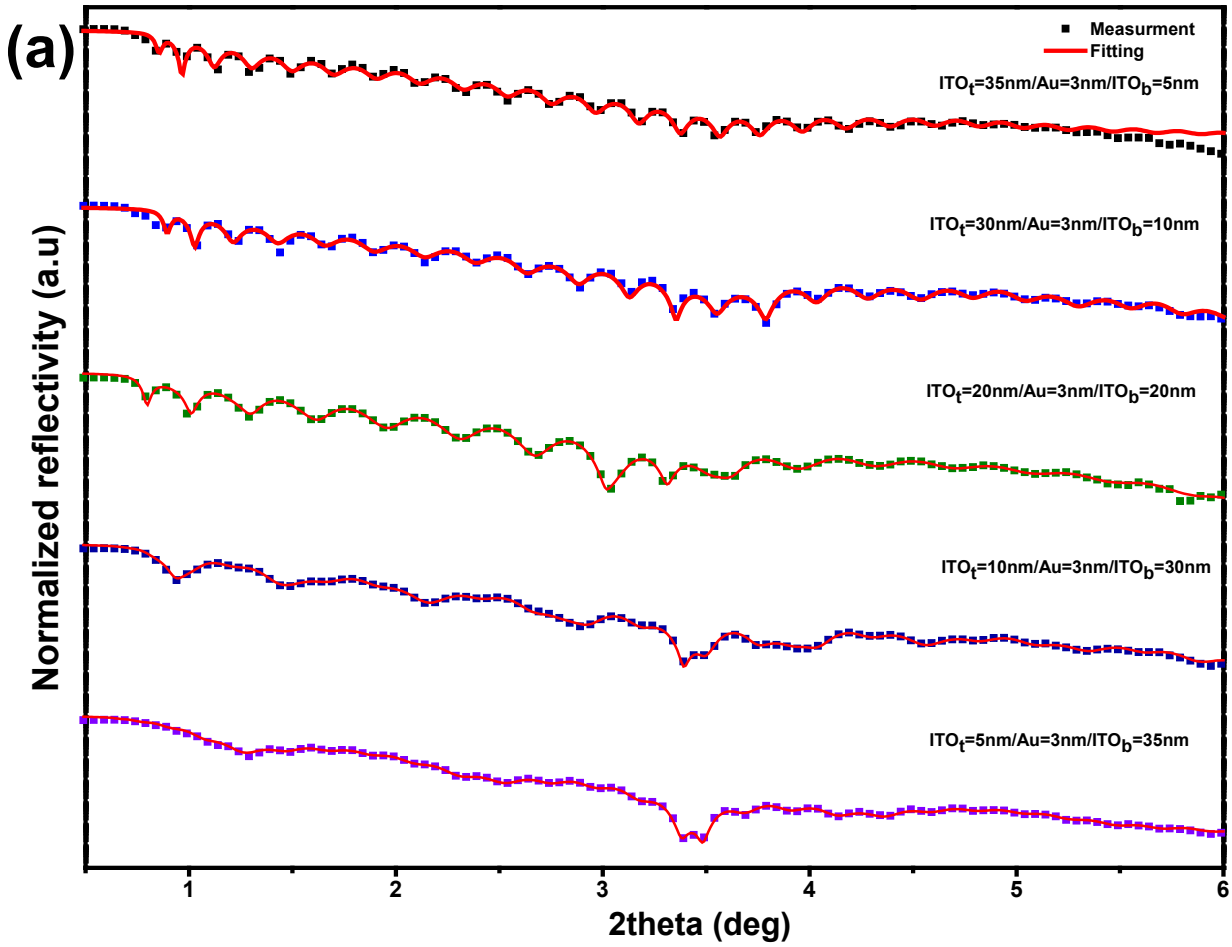
(a)
Measurment
Fitting
ITO$_t$=35nm/Au=3nm/ITO$_b$=5nm
ITO$_t$=30nm/Au=3nm/ITO$_b$=10nm
ITO$_t$=20nm/Au=3nm/ITO$_b$=20nm
ITO$_t$=10nm/Au=3nm/ITO$_b$=30nm
ITO$_t$=5nm/Au=3nm/ITO$_b$=35nm
Normalized reflectivity (a.u)
1
2
3
4
5
6
2theta (deg)

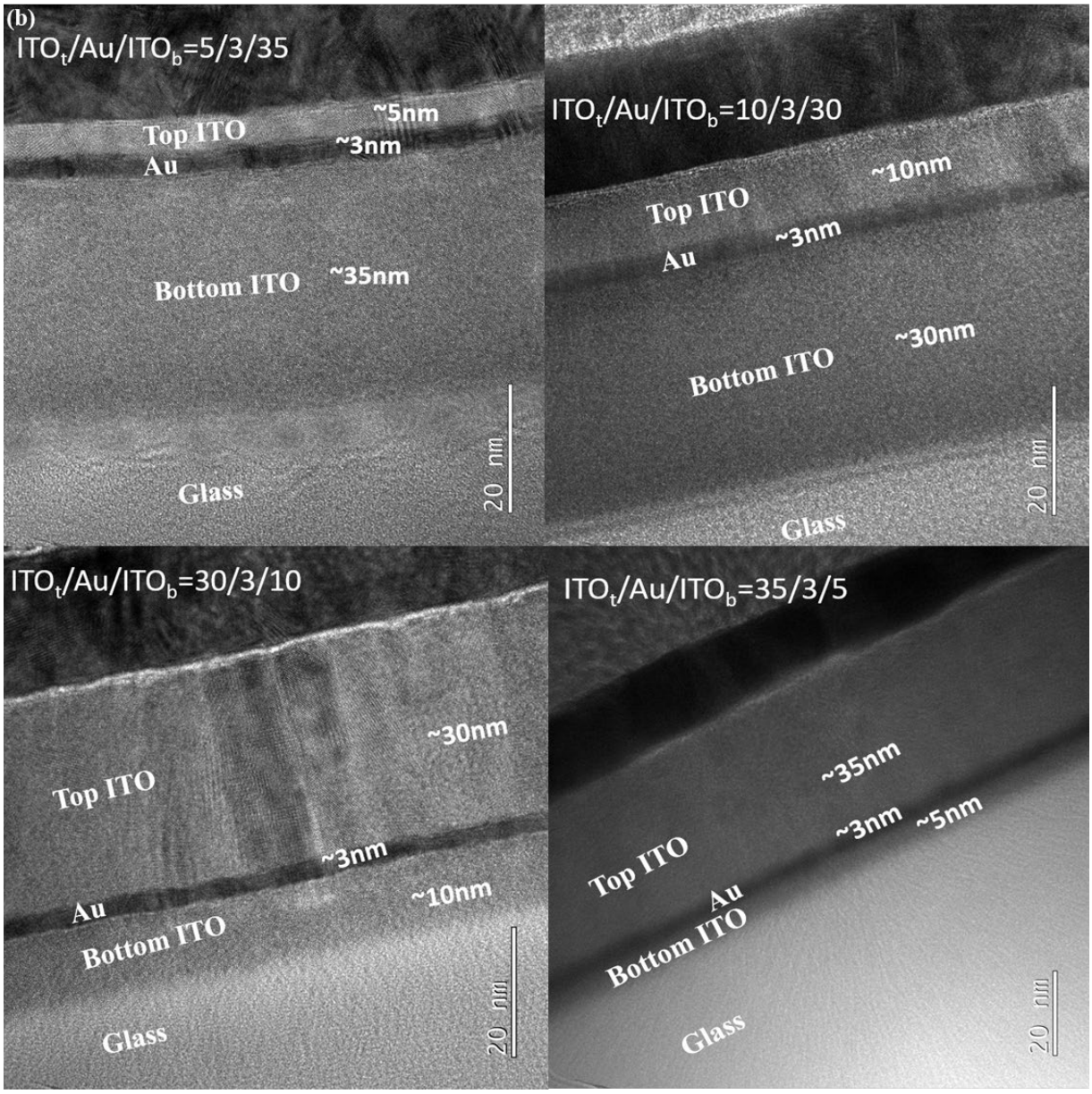

Figure 2(a) Measured (symbols) and fitted (solid lines) XRR pattern of ITO (t nm)/Au (2.9 nm)/ITO (40-t nm) trilayer films with different values of top layer thickness t. (Reprinted with permission from ACS Appl. Mater. Interfaces 2020, 12, 11, 13437–13446. Copyright © 2020 American Chemical Society) (b) Cross section TEM micrographs of four trilayer samples

In the optical measurement, total internal reflection ellipsometry (TIRE) was employed to reveal the optical as well as the plasmonic properties of the ITO/Au/ITO trilayer structures. The Kretschmann configuration[21] was employed to measure the variable angle ellipsometric

parameters $tan\,\psi$ as well as $\Delta(\lambda)$, where the physical originality of the obtained ellipsometric angles $\psi(\lambda)$and $\Delta(\lambda)$ represent the reflectance amplitude ratio and the phase difference between the p- and s- polarized light respectively, as shown in Equation (1)[22]:

$$\frac{R_p}{R_s} = tan\,\psi e^{-i\Delta} \quad (1)$$

Here, R_p and R_s are the experimental measured reflection coefficients for the p– and s– polarized light, respectively. In the measurement, BK-7 index matching liquid (n=1.5167; Cargille Laboratory) was added between the prism/glass interface as a liquid coupler to fill in the air gap between prism and glass. A glycerin layer (one kind of the sampling liquids that has been used in the experiment) was placed at the bottom as a sampling layer for surface plasmon resonance (SPR) detection similar to many bio-detection technique[23-25].

Figure 3(a) shows the $tan\,\psi$ curves of the five asymmetric trilayer samples with various incident angles, ranging from 40° to 60° at a 2° angle increment. The spectral reflectivity curves with different angles of incident are represented by color gradient i.e., the red curve indicates the 40° angles of incident and the blue corresponds to the 60°. Generally speaking, HMM supports various plasmonic modes including the surface and bulk plasmonic modes.[26] When the incident photon couples with the plasmon mode inside the HMM, the photon is absorbed either by the confined bulk mode or propagated surface mode along the interface.[27] Thus, both coupling modes will result in the reduction of the reflected beam intensity as its energy has been partially transmitted to the plasmons. Thus, the plasmonic resonance can be observed through the minimum positions in the reflectivity spectra i.e. reflectivity dip.[21, 24, 28] As shown in Figure 3(a), two reflectance dips are observed from the $tan\,\psi$ curves in the measured spectral range (only the 400 nm to 1000 nm wavelength ranges are highlighted, the full spectra can be found in the supporting information.)

representing the difference modes which are denoted as pseudo-Brewster (PB) and bulk plasmon-polariton (BPP) in the visible and NIR ranges, respectively.

The PB reflectance minima have been reported by Bello et. al. in similar trilayer system which contains a thin layer of high refractive index inserted between two ITO layers.[29] As shown in Figure 3, PB reflectance dips of different incident angles (the movement of dips indicated by the navy blue arrow) span a wide wavelength range from approximately 580 nm to 400 nm, showing a strong angular dependency. The dip point shifts to shorter wavelength continuously when the light incident angle is increased. When angle of incident (AOI) exceeds 50^{o}, the dip seems to be disappeared due to the fact that the dip position is located out of our measuring range (i.e. < 400 nm). The originality of the PB mode reflectance dip corresponds to the pseudo-Brewster angle, which is the analogy of conventional Brewster angle i.e. the reflected p-polarized light becomes zero. However, for lossy media, the complete cancelation of reflected p-polarized light may not be existed at the Brewster angle. Therefore, a more general definition is the pseudo-Brewster angle θ_{PB} which is the incident angle when the reflected p-polarized light attains a minimum. Thus, the $\tan(\psi)$ minima observed in short wavelength range are arisen from the minimizing of the p-polarized light due to the pseudo-Brewster angle[30-31]

To further explain the tendency of the $\tan(\psi)$ minima go to shorter wavelength as the incident angle becomes larger, we may consider the optical loss from the system either on the trilayer or the sampling liquid. Studies have reported that the pseudo Brewster angle will increase with a larger loss in optical lossy media (or larger imaginary part in the complex refractive index n'' where $N = n' + in''$).[31] From our experimental results, we observe that for larger incident angle, the wavelength that attains the Brewster effect shifts to shorter wavelength position. The shift of

the PB mode is caused by the optical loss of the sampling liquid (glycerin) at high photon energy range.

The second $tan\,\psi$ dip point is observed at the NIR range (marked as BPP mode and labeled by red dotted lines in Figure 3(a)). Unlike the PB mode, the BPP mode is independent of the light incident angle. The BPP reflectance dips are originated from the strong optical mode confinement inside the HMM structures, which is the hybridization of short-range surface plasmon polaritons at the two metal-dielectric interfaces.[32] As the inserted gold film thickness (~3 nm) is much smaller than the skin depth of the surface plasmon modes on both top and bottom ITO-Au interfaces, the top and bottom plasmonic modes will couple one another to become a collective charge oscillation within the trilayer, forming the observed BPP mode.[33] Compared to the reflectance dips arisen from the conventional surface plasmon mode which is angular dependent, the BPP mode is slightly different to the surface mode that the dip points arisen from BPP mode are highly localized without any angular dependencies. This anomalous reflectance minima of p-polarized light in oblique incidence angle can only be observed by the coupling of prism or gratings in multilayers HMM due to the momentum matching requirements. With the assistance of the cosΔ spectra in Figure 3(a), the reflectance dip points originated from the plasmonic resonance can be confirmed by the rapid phase change from 1 (Δ= 0^o) to (Δ= 180^o or π) reflectance minimum was attained.[34-35]

For better interpretation of the variation of the angular dependent reflectivity among different samples, the variable-angle spectroscopic ellipsometry (VASE) 3d contour color plots are shown in Figure 3(b). In the figure, color gradient (as shown in the inserted bar) is used to indicate the value of $tan\,\psi$ ranging from 0 (minimum) to 1(maximum). From the profiles, we notice that as the thickness of the top ITO layer increases, the position of the observed PB and BPP mode reflectivity minima shifts upward i.e. the PB mode moves toward the upper left corner with the

violet color gradably fading away. This means that the PB mode is blue shifting with increasing top ITO layer thickness and this dip is moved profoundly to larger AOI. Similar variation can also be observed in the BPP mode, where the BPP dip moving upward when the top ITO thickness increases. However, the BPP dip does not show any angular dependency, i.e. it is localized at approximately between 760 nm and 820 nm for $ITO_t/Au/ITO_b$ = 5/3/35 (nm) sample to ITOt/Au/ITOb = 35/3/5 (nm). Our results indicate that a smaller AOI is required to excite the plasmon modes when the thin gold layer is closer to the sensing liquid. For example, the gold layer of the $ITO_t/Au/ITO_b$ = 5/3/35 (nm) sample holds the closest distance from the sampling liquid, showing the lowest (the smallest $tan\,\psi$ value throughout the measured incident angle) and the sharpest (the smallest half width value) $tan\,\psi$ dip among the five samples. The short penetration depth and high-k mode properties are the reason that BPP mode can penetrate deep into the sampling liquid, resulting in a strong coupling. For samples with thicker top ITO layer, the Au interface is relatively far away from the bottom liquid. A larger incident angle is required in order to give raise to higher k-vector to excite the BPP mode. This explains why the BPP dip can only be observed at larger incident for ITOt/Au/ITOb = 35/3/5 (nm) sample and the value of BPP dip reflectance become smaller at increased incident angle. Among the five samples, the $ITO_t/Au/ITO_b$ = 5/3/35 (nm) sample have the optimal geometry that allows the BPP mode couple better with the liquid at the bottom to achieve the lowest reflectivity at 760 nm, and the average half-width value of the sharpest BPP dip extends approximate 100 nm which shows a relative board-band anti-reflection ability among the five samples. These findings give us a new possibility to design a spectral selected antireflection coating through thickness controlling of the layers.

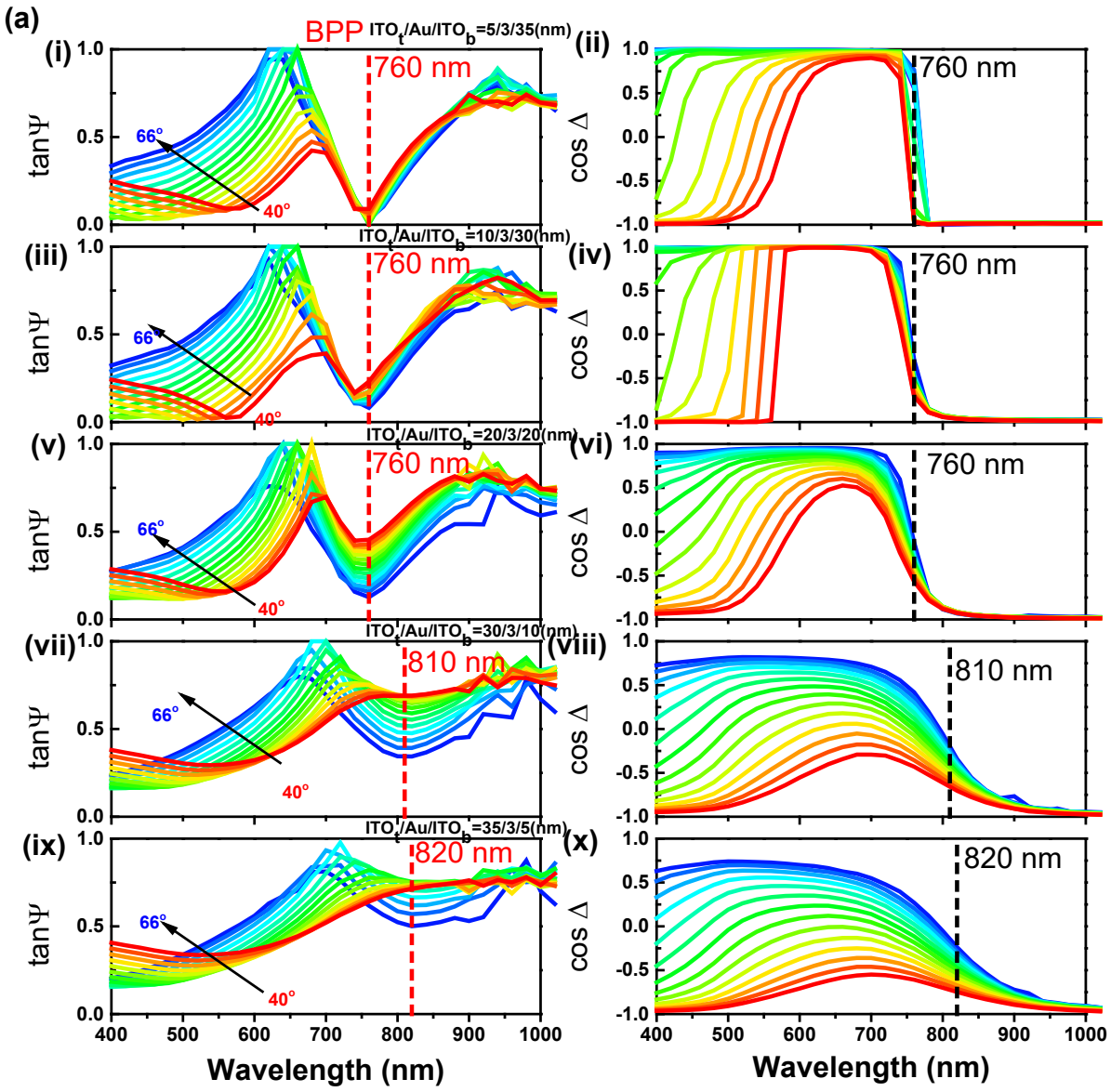
(a)
BPP ITO$_t$/Au/ITO$_b$=5/3/35(nm)
(i)
(ii)
760 nm
tanΨ
cos Δ
66°
40°
ITO$_t$/Au/ITO$_b$=10/3/30(nm)
(iii)
(iv)
ITO$_t$/Au/ITO$_b$=20/3/20(nm)
(v)
(vi)
ITO$_t$/Au/ITO$_b$=30/3/10(nm)
(vii)
(viii)
810 nm
ITO$_t$/Au/ITO$_b$=35/3/5(nm)
(ix)
(x)
820 nm
Wavelength (nm)

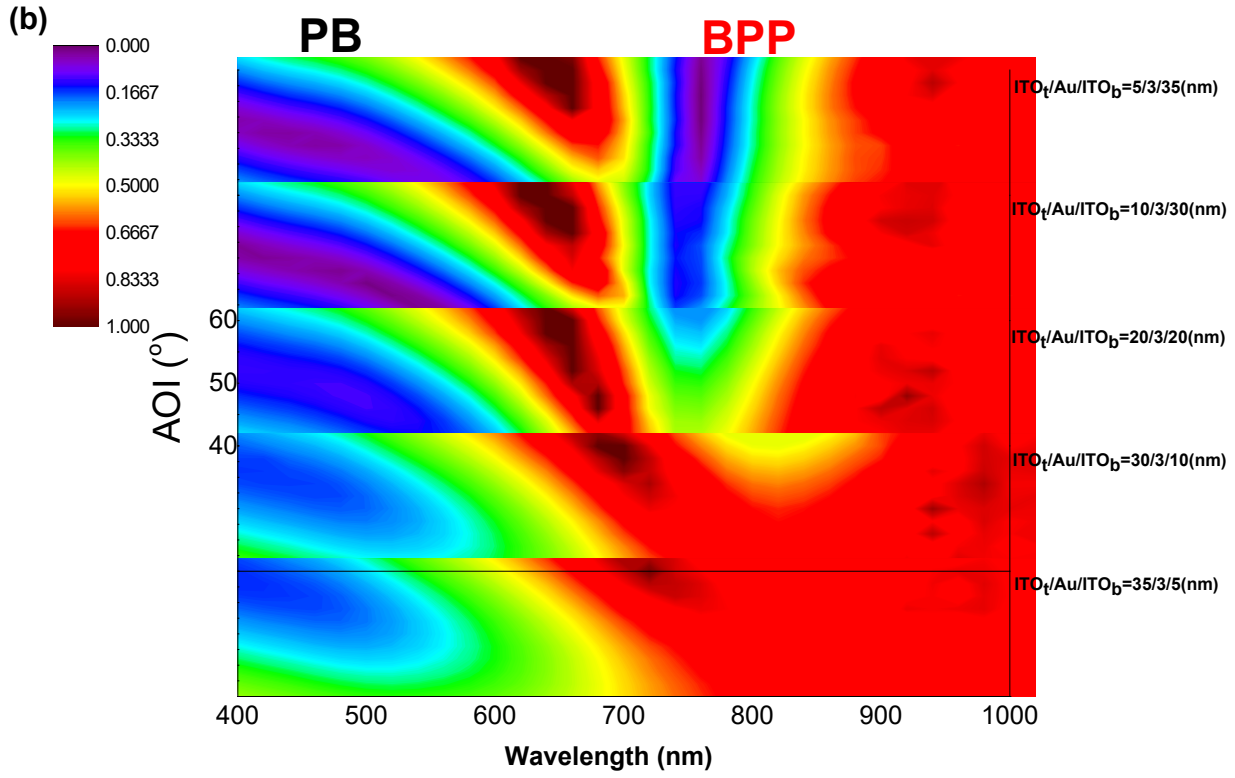

Figure 3(a) Reflectivity spectra of five asymmetric samples angles of incidence from 40°(red) to 60° (blue) with Each color change represents an angle increment of 2°. (b) 3D contour map of Reflectivity profile of all five asymmetric samples as a function of incident (from 40° to 65°) wavelength and angle of incident.

To fully realize the reflectivity profile, a simulation, modelled using Fresnel equations as described by Rhodes et al. and Losego et al.[36-37], was calculated to demonstrate the reflectance at each interface. In the simulation, we assumed that the sample was a three-layer structure with the schematic diagram shown in Figure 4. The detailed calculation was shown in the supplementally data file. On the basis of the simulation of Fresnel reflectance equations, the response of the ellipsometry parameters ($\tan\psi$) can also be calculated. However, before obtaining the simulated

reflectivity spectra (R_p/R_s), we needed to input several parameters namely, the optical permittivities of the three layers, into the equations (S2) -(S6) in the supplementally information. Figure 5 shows the real and imaginary part of the pseudo-permittivity of the five asymmetric trilayer sample with three different incident angles (40º, 50 º and 60º). These optical permittivities (or dielectric constants) are the parameters obtained simultaneously from the ellipsometry measurements. The permittivity profiles are then imported into the Fresnel reflectance program and output as the reflectance spectra. The optical permittivities shown in Figure 5 represent the "pseudo" dielectric function which are calculated reversely from the $\psi(\lambda)$and $\Delta(\lambda)$ data based on Fresnel formalism.[38] In some cases, it cannot completely reflect the intrinsic permittivities of the sample layer. Nevertheless, in our measurements, the prism, glass substrate and the glycerin layer are assumed to be transparent and non-absorbing material with zero extinction coefficient that does not contribute to the pseudo dielectric function in NIR range. Therefore, we believe that the change of the complex permittivity in Figure 5 can be accounted for the light-matter interaction of our IAI trilayer, and the pseudo dielectric function can be used to represent the permittivity of plasmonic trilayer to a certain extent.

In order to obtain the algorithm simulated reflectivity under this configuration, we assume that the incident light first travels through the transparent glass substrate (refractive index n=1.51), and then transmits to the IAI plasmonic trilayer with refractive index obtained from Figure 5 and the light finally travels through the semi-infinite thickness glycerin sensing media with constant refractive index 1.47. The light incident on the blackened sample stage is assumed to be totally absorbed and no light will be reflected back to the sample. Before entering into the glass substrate, the incident light passes through a right-angle prism. Thus, the incident angle is needed to be slightly adjusted due to the light bending properties, and the conversion between the external

incident angle and internal incident angle has been reported by Pluchery et al.[39] These corrections have been applied to obtain the simulated results which are plotted in Figure 6.

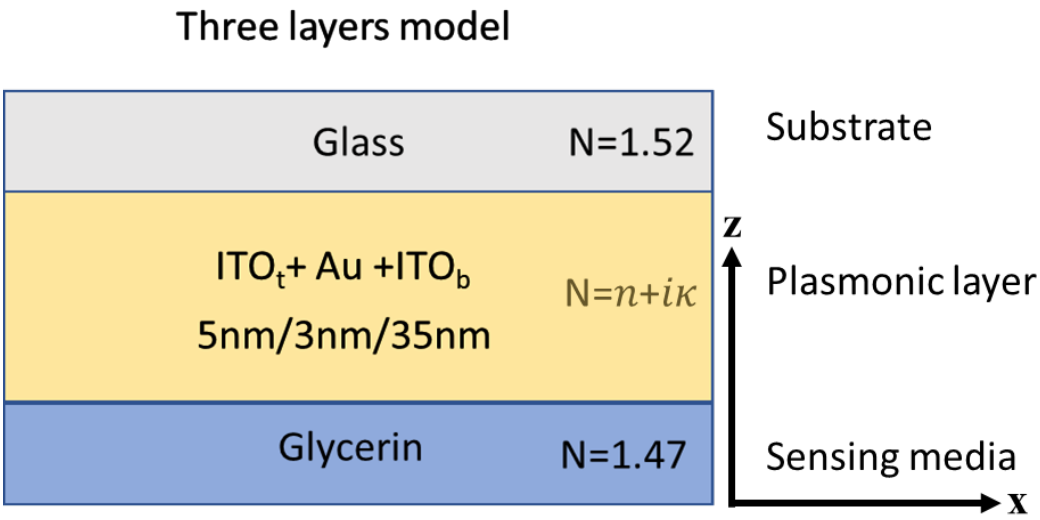

Figure 4 Schematic diagram of three-layers model for reflectance calculation.

In Figure 7, the simulated results resemble to the measured results, as the simulated reflectance dip positions almost coincide with the measured results (shown in Figure 3(a)). The major deviation between the measured and simulated spectra is in the visible wavelength. In the experimental spectra, there exists a dip due to the PB mode which is failed to be predicted in the simulated spectra. The monotonic growth of reflectance is observed in the simulated spectra. One of the possible reasons related to the sensing media. Since the glycerin is the sensing liquid in this configuration, which has a constant refractive index 1.47 throughout all the spectra range i.e. assuming the complex part of the refractive index is zero in the simulation. However, the complex part of refractive index (or extinction coefficient) in most of the materials will be nonzero or increased in high photon energy range due to the optical excitation or interband transition causing optical loss. This assumption may underestimate the nominal refractive index in the short visible

wavelength range during simulation. General speaking, although there is deviation in the visible range near UV, the overall simulation profiles match well with the measured profiles, especially, in the NIR range.

The optical properties of plasmonic layer can be revealed from comparing the simulation and the measurement results. The experimentally obtained pseudo dielectric constant shows a classical Lorentzian oscillator response, and the oscillator strength (magnitude) increased with the incident angle observed in the y-axis in Figure 5 that the Lorentzian peak values increased with incident angle. The Lorentzian dielectric function of trilayers can only be probed under the prism coupled Kretschmann configuration because the plasmonic mode is being excited by the total internal reflected field and these observations possess totally different response compared with the ordinary ellipsometry measurement data (detailed in supplementary information Figure S5). The Lorentz-like response represents that the system consists of resonance effect when the incident light near the plasma frequency with respect to the Lorentz oscillator model. Notice that, the permittivity profile crosses the zero line at around 700 nm that coincide with the BPP mode in the reflectance spectra. This evidence confirm that the BPP mode is actually originate from the ENZ permittivity.[40]

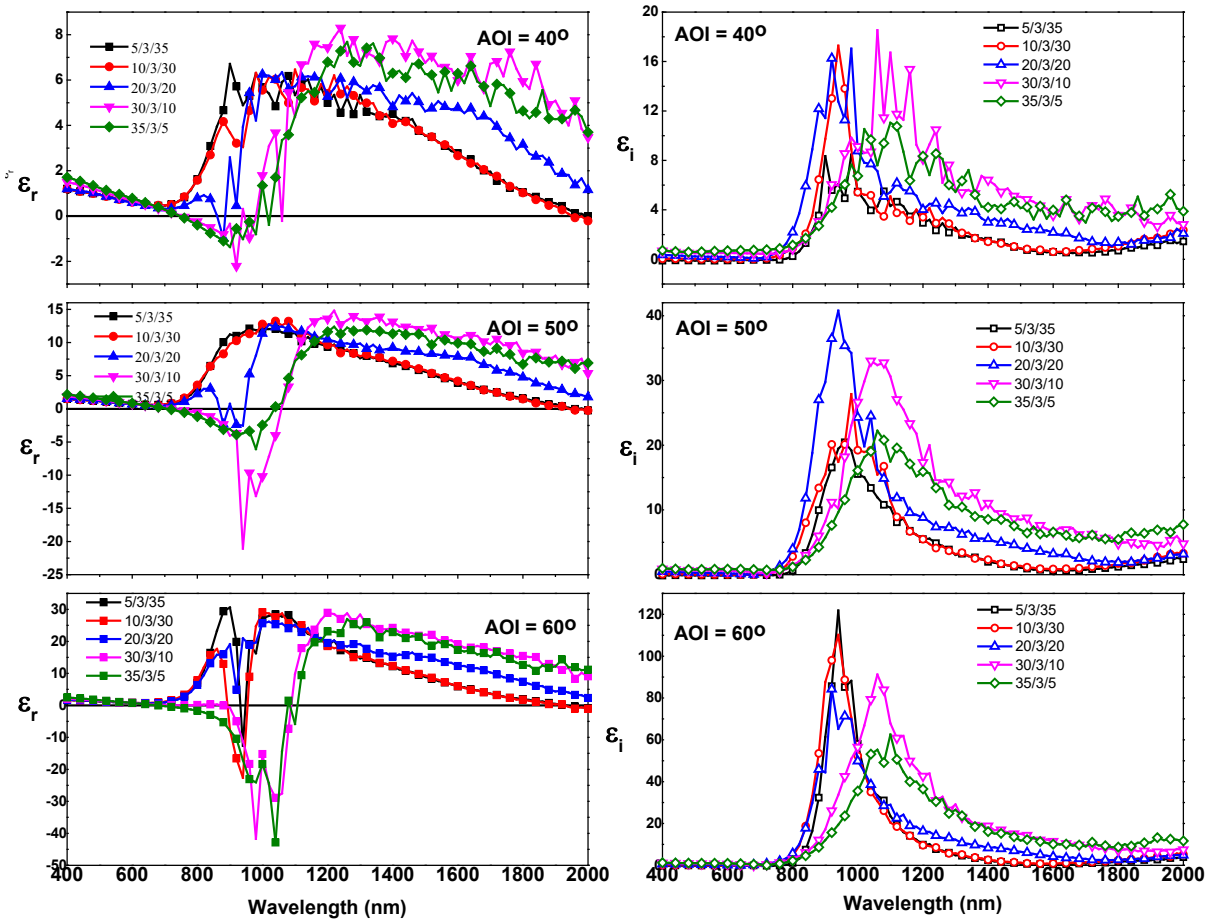

Figure 5 real and imaginary permittivity of five asymmetric layer sample with 40°, 50° and 60° incident angle.

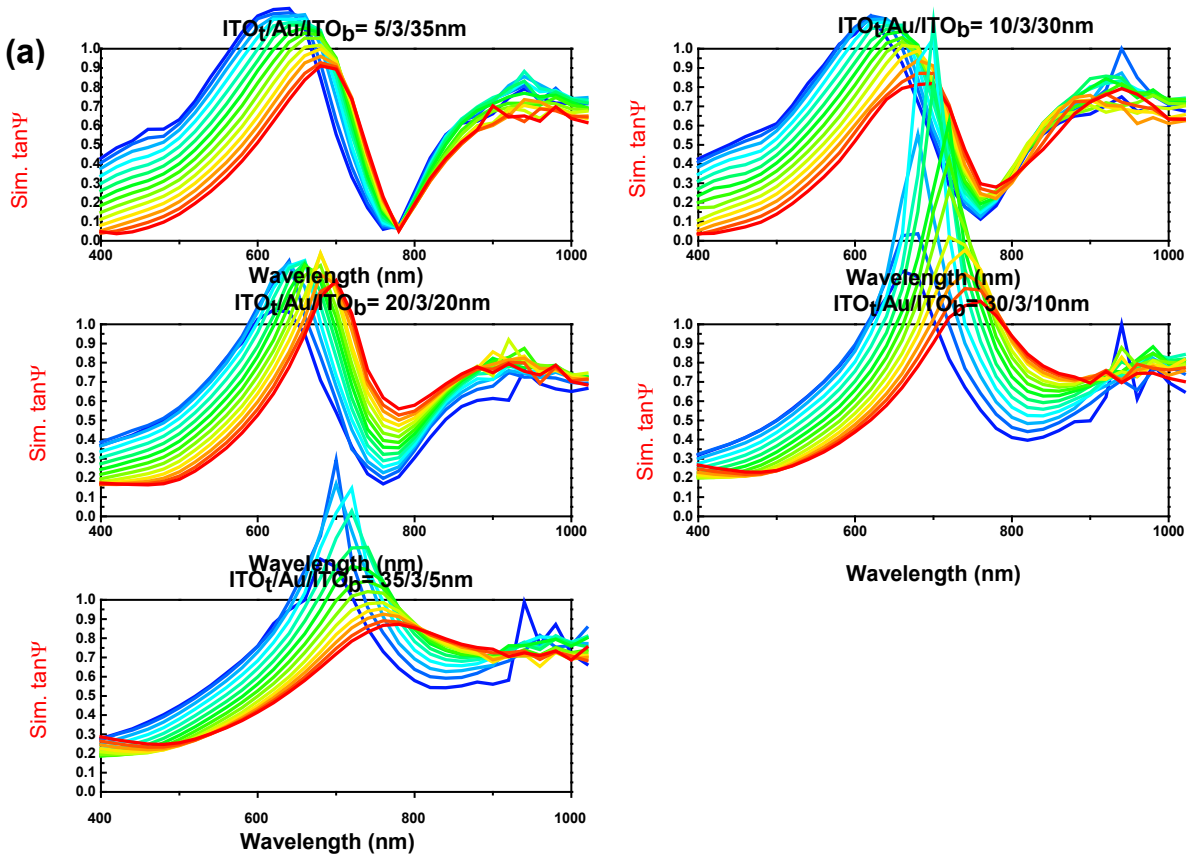
(a)
ITOt/Au/ITOb= 5/3/35nm
ITOt/Au/ITOb= 10/3/30nm
ITOt/Au/ITOb= 20/3/20nm
ITOt/Au/ITOb= 30/3/10nm
ITOt/Au/ITOb= 35/3/5nm
Sim. tanΨ
Wavelength (nm)

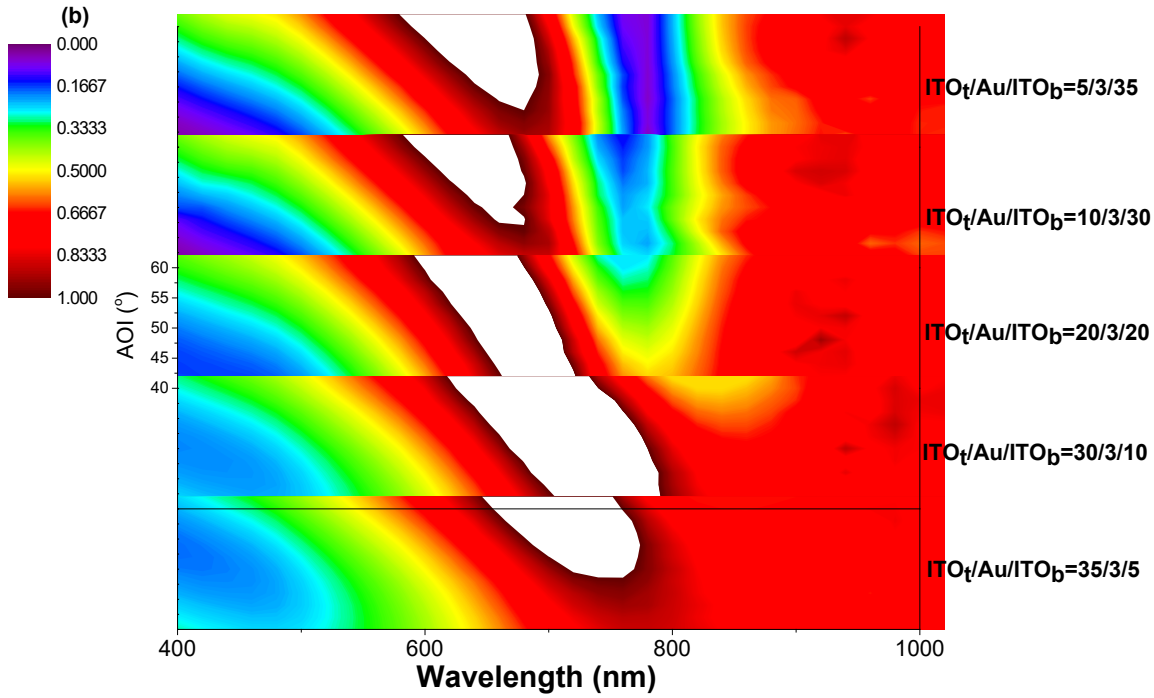

Figure 6(a) Simulated reflectivity profile of ITOt/Au/ITOb asymmetric samples from 40º to 60º AOI with Each color change represents an angle increment of 2°. (b) 3D contour map of Reflectivity profile of all five asymmetric samples as a function of incident (from 40° to 60°) wavelength and angle of incident.

In order to reveal the dispersion relation of the samples, we calculated the dispersion relation of surface plasmon on the metal and dielectric interfaces using equations (2) and (3) based on solving the Maxwell' equation with suitable boundary conditions[41]. Figure 7 shows the calculated surface plasmon dispersion curves of trilayer/glass interfaces of different asymmetric samples.:

$$\mathrm{k}_{sp} = \frac{\omega}{c}\sqrt{\frac{\varepsilon_{\mathrm{m}}\varepsilon_{\mathrm{d}}}{\varepsilon_{\mathrm{m}}+\varepsilon_{\mathrm{d}}}} = k'_{sp} + ik''_{sp} \qquad (2)$$

$$k_x = \frac{\omega}{c} n_{glass} \sin\theta \qquad (3)$$

where k_{sp} is the surface plasmon wave vector on x-direction. It can be derived by using the complex permittivity metallic layer ε_{m} which is the permittivity of the trilayer shown in Figure 5

and the permittivity of the dielectric (glass) ε_d. k_x is the wave vector horizontal component of the incident light, it can be determined by the incident angle θ and the refractive index of glass substrate (n_{glass}=1.51), The complex permittivity was then used to calculate the dispersion relationship of the asymmetric trilayer samples. Inset in Figure 7 shows the enlarged view of the intersection point of the free space light with incident angle of 56° to the samples. The intercept of the light line and the dispersion curve represents the plasmon resonance energies listed in Table 1, and the resonance wavelength coincides with the second reflectivity dip wavelength measured in Figure 3(a). It is believed that the second reflectivity dip was caused by the coupling of incident photon and the plasmonic mode.

Table 1 The cross point of dispersion curve of five IAI samples with the incident wave vector k_x.

ITO_t/Au/ITO_b Samples	Resonance energy (eV)	Wavelength(nm)
5/3/35	1.632	759.707
10/3/30	1.621	764.862
20/3/20	1.620	765.335
30/3/10	1.573	788.202
35/3/5	1.609	770.567

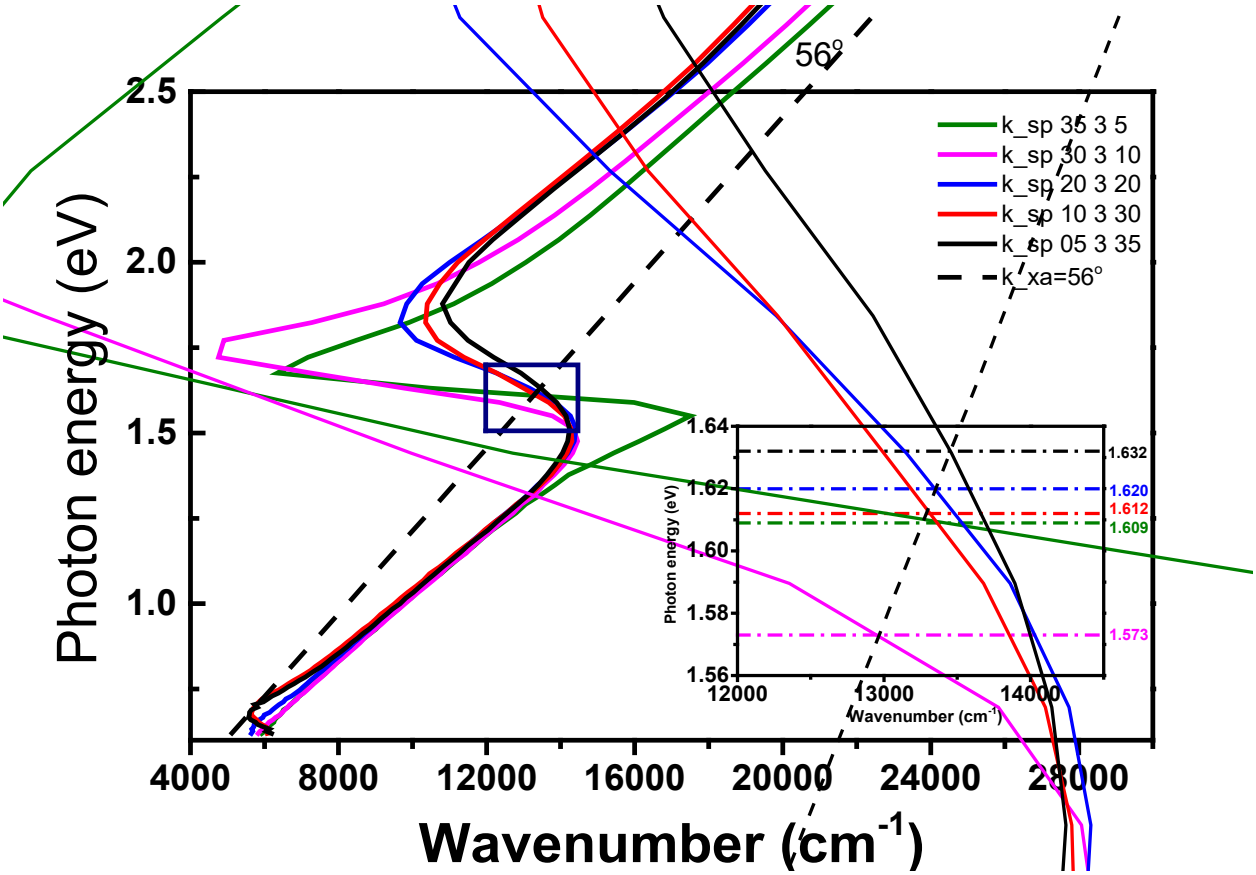

Figure 7 surface plasmon dispersion curve of trilayer/glass interfaces with asymmetric samples. The black dashed line represents the light-line with incident angle 56°. The inset shows the enlarged view of trilayer/glass interfaces surface plasmon dispersion curve. The surface plasmon resonance energy indicated by the dash-dot lines.

In order to investigate the effects of the sampling liquid on the reflectance spectra, various sampling liquids (besides glycerin) including paraffin oil, isopropyl alcohol (IPA), ethanol and deionized water have been employed. These sampling liquids possess different refractive indices ranging from 1.48 to 1.33, and act as the sensing media which will couple with the plasmon in the trilayer thin film. The $ITO_t/Au/ITO_b$ = 5/3/35 (nm) sample under attenuated-total-reflection (ATR) (or Kretschmann) mode with light incident angle 50° and 60° in contact with different types of sampling liquids was employed to investigate this relation. In the ATR configuration, the sample

was flipped such that the conductive plasmonic trilayer was in-contact with the liquid being sensed. The plasmon excitation on Kretschmann configuration within the metal and sampling interface is called the Multi-Parametric Surface Plasmon Resonance (MP-SPR)[42]. The position of $\tan\psi$ minimum changes with the refractive indices of the sampling liquids as shown in Figure *8*(a). The reflectivity dip right shifts from 740 nm to 830 nm as the refractive indices of the sampling liquids increase from 1.33 to 1.48. From the figure , it is noticed that the dip positions of $\tan\psi$ seem to follow a linear relationship with the refractive indices of sampling liquids. Thus, a calibration curve can be obtained by the linear regression method for liquid sensing as shown in Figure *8*(c). On the basis of our measurement, it is shown that we can use the ITOt/Au/ITOb = 5/3/35 (nm) trilayer sample as a passive sensing element to measure unknown refractive index of any liquid through locating the dip position of the BPP mode. The sensitivity of this sensing method is represented by the slope of the linear fitted line which the $dn/d\lambda$ in this case possesses an accuracy up to 0.00181 refractive index unit (RIU) per nm i.e. the sensing accuracy or the sensitivity of this structure is 552 nm/RIU, which is comparable to other novel reported MIM waveguide type sensor (approximate 550 nm/RIU [43]). Furthermore, the design can be optimized by adding more stacking ITO/Au layers to reduce the FWHM value of the BPP mode. Noticed that the plasmonic effect is significantly enhanced when the gold content is increased, however it will also accompany with larger optical loss. The control of the plasmonic resonance wavelength and reduce the optical loss is still a challenging job in this field. Our results demonstrated that this IAI structure can be used to measure the refractive index of any liquid, and this technique will provide a new pathway for the development of RI-sensor or biosensor using the surface plasmon enhances the sensitivity of ellipsometry.

Another advantage of using BPP mode as the detection of unknown refractive index because this mode is independent of angle of incident, indicating that the IAI trilayer as the active element of the sensor chips will possess a high angular stability for optical measurement i.e. small angular variation will not affect the result of detection. Once the dip position is calibrated with a known index solution, any small change in refractive index (for example, the existence of dopant inside the solution) will be detected. This will potentially provide a simple and wasteless method for testing drug as well as the virus like Covid-19 since the test only requires a droplet of solution[25].

Figure 9 shows the measured $\tan\psi$ results for all the sampling liquids under different angles of incident. It is noticed that the reflectivity dip positions are almost the same and independent to the incident angle of light. It is believed that the originality of reflectivity dip is the resonant effect of ENZ frequency (or crossover wavelength λ_p) and this crossover wavelength will be blue shifted or shifted to shorter wavelength as the refractive index of the contact media increase. This can be deduced from the linear calibration curve of the dip position against refractive index of sensing media. When the refractive index of air ($n_a \approx 1.0003$) is put into the equation, the calculated trough position wavelength is approximately 1009 nm. It is believed that the trough position echo with the crossover wavelength reported in previous studies[16] when the sampling media is air or in the so-called air-coupling configuration reported[44]. ($n_a \approx 1$)

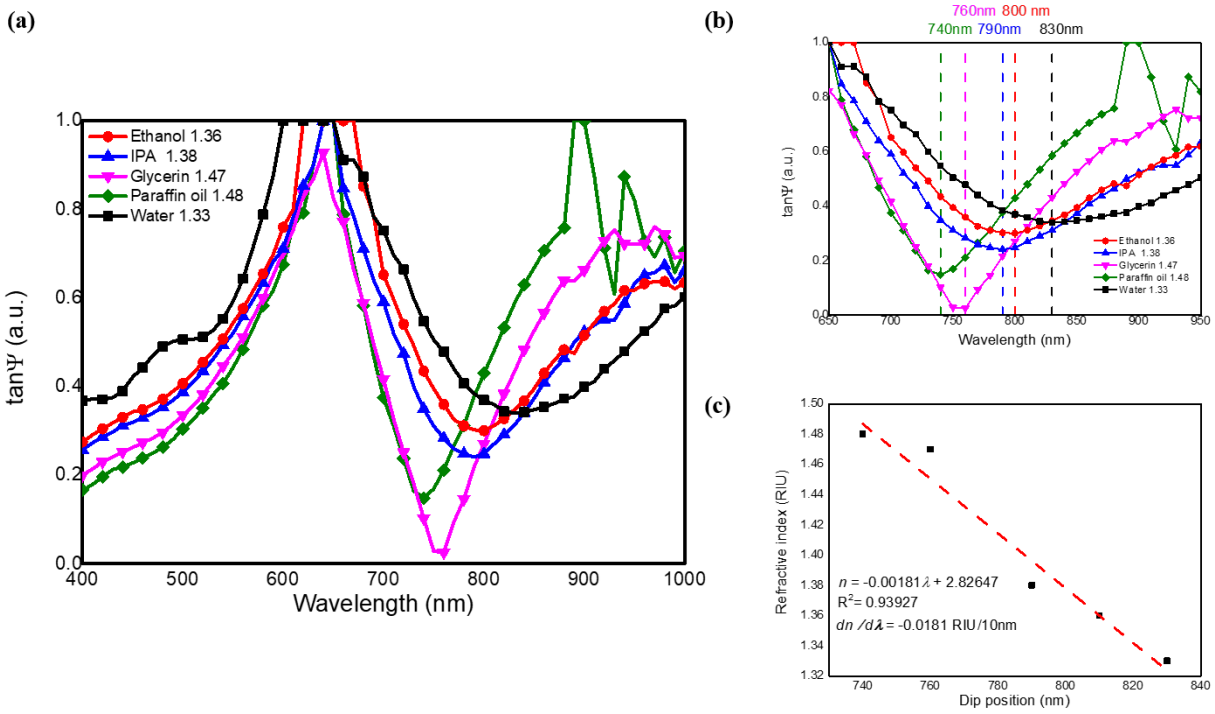

Figure 8 (a) Total internal reflection ellipsometry (TIRE) measured tanψ against wavelength of ITOt/Au/ITOb = 5/3/35 (nm) sample with various liquids as sampling medium under angle of incident (AOI) =60º. (b) the enlarged view locating the dip position from different sample liquid, (c) plot of dip position vs refractive index for different sampling liquids.

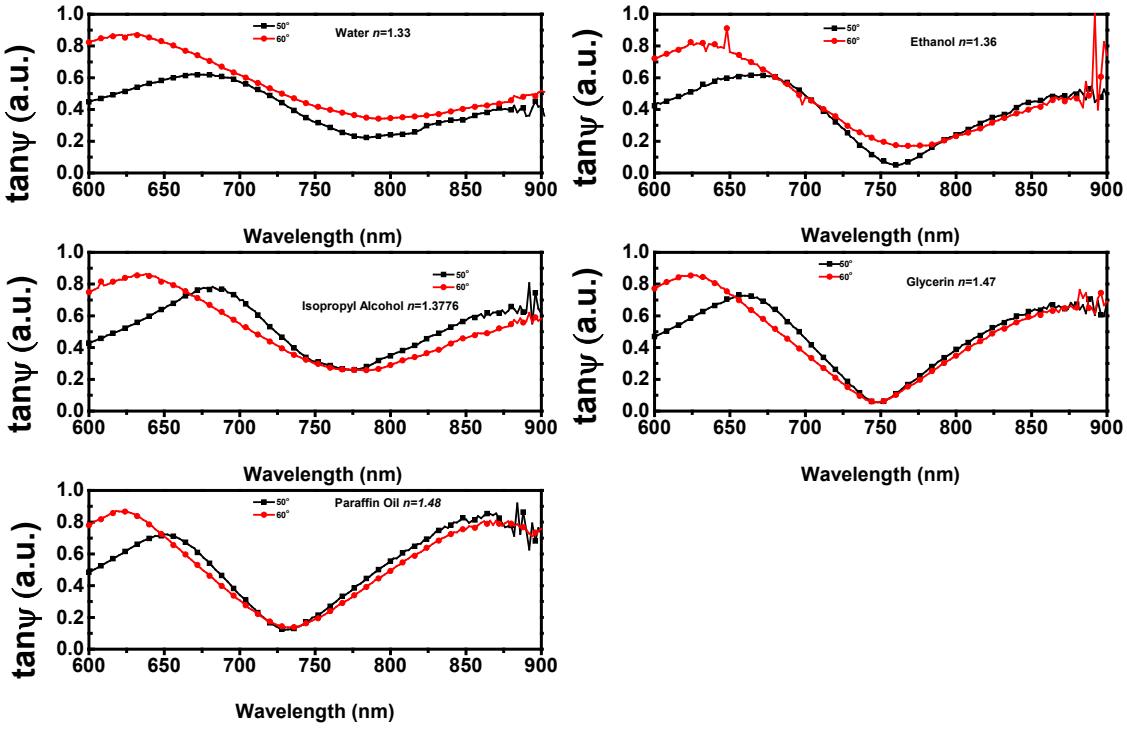

Figure 9 Measured tanψ curve by Kretschmann configuration with 50° and 60° incident angles by sensing various types of liquid including paraffin oil, glycerin, isopropyl alcohol (IPA) ethanol and deionized water.

CONCLUSION

Five IAI trilayer samples, with constant 40 nm total ITO thickness and 3 nm gold layer but with different top and bottom ITO thicknesses, have been fabricated using magnetron sputtering. The XRD and TEM characterization results demonstrate that the position of the Au inserted layer can be precisely controlled. The reflectivity spectra under different incident angles gives the information of the plasmonic properties within the trilayers by studying the reflectance dips position. The minima, corresponding to the pseudo-Brewster (PB), bulk plasmon-polariton (BPP)

and surface plasmon-polariton (SPP_{ITO}) modes are observed from the reflectance spectra. The position of the first and the last modes are strongly dependent on angle of incident, while the second one is independent on the angle of incident. The sharpness of the BPP dips is highly dependent to the distance of the Au/ITO_t interface to the liquid inserted below. The position of the BPP mode is highly depended on the refractive index of the sampling liquid. The obtained experimental spectra are confirmed by the simulation based on the Fresnel reflection theory. The numerical result shows a good agreement with the measured spectra to confirm the plasmonic resonance properties. Finally, the ITO_t/Au/ITO_b = 5/3/35 (nm) are used as a passive liquid sensing element for measuring the refractive index of unknown liquid. The sensing accuracy obtained is 552 nm/RIU. Our results demonstrate the potential application in drug and/or virus testing by using this IAI trilayer for plasmonic enhanced refractive index sensor measurement with high angular stability.

ASSOCIATED CONTENT

Corresponding Author

*CLM.: e-mail, apaclmak@polyu.edu.hk; phone, (852)2766 5667; fax, (852)23337629.

ACKNOWLEDGMENTS

The First Author Ka Kin Lam was supported by The Hong Kong Polytechnic University (ZVGH).

Supporting Information

The supporting information is including the additional measurements of dielectric constant of trilayer structures (to determine the complex permittivity of trilayer samples and fit with suitable

optical model.) to retrieve the optical properties of five samples. Also, the TIRE measurements were performed with ITO film, Au/ITO bi-layer and trilayer with same overall thickness to demonstrate the BPP mode only existing in trilayer structures and the full reflectivity spectra of five trilayer samples showing the additional mode corresponding to the bottom ITO in NIR range. Finally, the mathematical calculation of internal reflection angle with the light oblique incident into a right-angle prism.

REFERENCES

1. Li, S.; Zhao, W.; Sun, Y.; Dai, N.; Hu, G., High-Efficiency, Low-Cost Distributed Bragg Reflector Based on Al2o3/Pbzr0.4ti0.6o3 Multilayer. *AIP Advances* **2020,** *10* (5), 055224.
2. Li, S.; Liu, K.; Long, X.; Chen, L.; Xie, Z.; Li, L.; Zhou, X., Numerical Study of Infrared Broadband Multilayer Film Absorber with Tunable Structural Colors. *Optics Communications* **2020,** *459*, 124950.
3. Abdelatty, M.; Badr, M.; Swillam, M., High-Speed Hybrid Plasmonic Electro-Optical Absorption Modulator Exploiting Epsilon-near-Zero Effect in Indium-Tin-Oxide. *Journal of Nanophotonics* **2018,** *12*, 1.
4. Liu, H.; Liu, P.; Bian, L.-a.; Chenxi, L.; Zhou, Q., Electro-Optic Modulator Side-Coupled with a Photonic Crystal Nanobeam Loaded Graphene/Al 2 O 3 Multilayer Stack. *Optical Materials Express* **2018,** *8*, 761.
5. Smolyaninov, I. I., Hyperbolic Metamaterial Geometries and Basic Properties. In *Hyperbolic Metamaterials*, Morgan & Claypool Publishers: 2018; pp 1-1-1-6.
6. Jacob, Z.; Alekseyev, L. V.; Narimanov, E., Optical Hyperlens: Far-Field Imaging Beyond the Diffraction Limit. *Optics Express* **2006,** *14* (18), 8247-8256.
7. Kiba, T.; Yanome, K.; Kawamura, M.; Abe, Y.; Kim, K. H.; Takayama, J.; Murayama, A., Emission Enhancement in Indium Zinc Oxide(Izo)/Ag/Izo Sandwiched Structure Due to Surface Plasmon Resonance of Thin Ag Film. *Applied Surface Science* **2016,** *389*, 906-910.
8. Sreekanth, K. V.; Biaglow, T.; Strangi, G., Directional Spontaneous Emission Enhancement in Hyperbolic Metamaterials. *Journal of Applied Physics* **2013,** *114* (13), 134306.
9. Wan, M.; Gu, P.; Liu, W.; Chen, Z.; Wang, Z., Low Threshold Spaser Based on Deep-Subwavelength Spherical Hyperbolic Metamaterial Cavities. *Applied Physics Letters* **2017,** *110* (3), 031103.
10. Franzen, S.; Rhodes, C.; Cerruti, M.; Gerber, R. W.; Losego, M.; Maria, J.-P.; Aspnes, D. E., Plasmonic Phenomena in Indium Tin Oxide and Ito-Au Hybrid Films. *Opt. Lett.* **2009,** *34* (18), 2867-2869.
11. Khosroabadi, A. A.; Gangopadhyay, P.; Cocilovo, B.; Makai, L.; Basa, P.; Duong, B.; Thomas, J.; Norwood, R. A., Spectroscopic Ellipsometry on Metal and Metal-Oxide Multilayer Hybrid Plasmonic Nanostructures. *Opt. Lett.* **2013,** *38* (19), 3969-3972.
12. Guo, P.; Diroll, B. T.; Huang, W.; Zeng, L.; Wang, B.; Bedzyk, M. J.; Facchetti, A.; Marks, T. J.; Chang, R. P. H.; Schaller, R. D., Low-Loss near-Infrared Hyperbolic Metamaterials with Epitaxial Ito-In2o3 Multilayers. *ACS Photonics* **2018,** *5* (5), 2000-2007.
13. Han, L.; Ding, H.; Huang, T.; Wu, X.; Chen, B.; Ren, K.; Fu, S., Broadband Optical Reflection Modulator in Indium-Tin-Oxide-Filled Hybrid Plasmonic Waveguide with High Modulation Depth. *Plasmonics* **2018,** *13* (4), 1309-1314.
14. Shi, K.; Haque, R. R.; Zhao, B.; Zhao, R.; Lu, Z., Broadband Electro-Optical Modulator Based on Transparent Conducting Oxide. *Opt. Lett.* **2014,** *39* (17), 4978-4981.
15. Fang, X.; Mak, C. L.; Dai, J.; Li, K.; Ye, H.; Leung, C. W., Ito/Au/Ito Sandwich Structure for near-Infrared Plasmonics. *ACS Applied Materials & Interfaces* **2014,** *6* (18), 15743-15752.
16. Lam, K. K.; Ng, S. M.; Wong, H. F.; Fei, L.; Liu, Y.; Chan, K. H.; Ye, H.; Leung, C. W.; Mak, C. L., Effect of Thickness on the Optical and Electrical Properties of Ito/Au/Ito Sandwich Structures. *ACS Applied Materials & Interfaces* **2020,** *12* (11), 13437-13446.
17. Wu, K.; Wang, Z.; Yang, J.; Ye, H., Large Optical Nonlinearity of Ito/Ag/Ito Sandwiches Based on Z-Scan Measurement. *Opt. Lett.* **2019,** *44* (10), 2490-2493.

18. Chen, C.; Wang, Z.; Wu, K.; Chong, H.; Xu, Z.; Ye, H., Ito–Tin–Ito Sandwiches for near-Infrared Plasmonic Materials. *ACS Applied Materials & Interfaces* **2018,** *10* (17), 14886-14893.
19. Menchini, F.; Serenelli, L.; Stracci, G.; Izzi, M.; Salza, E.; Caputo, D.; Cesare, G. d.; Tucci, M. In *Temperature Effects on Sputtered Ito*, 2018 IEEE 7th World Conference on Photovoltaic Energy Conversion (WCPEC) (A Joint Conference of 45th IEEE PVSC, 28th PVSEC & 34th EU PVSEC), 10-15 June 2018; 2018; pp 3128-3132.
20. Poulopoulos, P.; Grammatikopoulos, S.; Trachylis, D.; Bissas, G.; Dragatsikas, I.; Velgakis, M.; Politis, C., Growth and Optical Properties of Nanocrystalline Titania Films for Optoelectronics and Photovoltaics. *Journal of Surfaces and Interfaces of Materials* **2015,** *3*, 52-59.
21. Arwin, H.; Poksinski, M.; Johansen, K., Total Internal Reflection Ellipsometry: Principles and Applications. *Appl. Opt.* **2004,** *43* (15), 3028-3036.
22. Fujiwara, H., Introduction to Spectroscopic Ellipsometry. In *Spectroscopic Ellipsometry*, 2007; pp 1-11.
23. Chlpík, J.; Bombarová, K.; Cirak, J., *Total Internal Reflection Ellipsometry in the Investigation of Phenomena at Surfaces and Interfaces for Biosensing*. 2014; p 275-278.
24. Balevicius, Z.; Paulauskas, A.; Plikusiene, I.; Mikoliunaite, L.; Bechelany, M.; Popov, A.; Ramanavicius, A.; Ramanaviciene, A., Towards the Application of Al2o3/Zno Nanolaminates in Immunosensors: Total Internal Reflection Spectroscopic Ellipsometry Based Evaluation of Bsa Immobilization. *Journal of Materials Chemistry C* **2018,** *6* (32), 8778-8783.
25. Plikusiene, I.; Maciulis, V.; Ramanaviciene, A.; Balevicius, Z.; Buzavaite-Verteliene, E.; Ciplys, E.; Slibinskas, R.; Simanavicius, M.; Zvirbliene, A.; Ramanavicius, A., Evaluation of Kinetics and Thermodynamics of Interaction between Immobilized Sars-Cov-2 Nucleoprotein and Specific Antibodies by Total Internal Reflection Ellipsometry. *Journal of Colloid and Interface Science* **2021,** *594*, 195-203.
26. Avrutsky, I.; Salakhutdinov, I.; Elser, J.; Podolskiy, V., Highly Confined Optical Modes in Nanoscale Metal-Dielectric Multilayers. *Physical Review B* **2007,** *75* (24), 241402.
27. Sreekanth, K. V.; De Luca, A.; Strangi, G., Experimental Demonstration of Surface and Bulk Plasmon Polaritons in Hypergratings. *Scientific Reports* **2013,** *3* (1), 3291.
28. Pant, U.; Mohapatra, S.; Moirangthem, R. S., Total Internal Reflection Ellipsometry Based Spr Sensor for Studying Biomolecular Interaction. *Materials Today: Proceedings* **2020,** *28*, 254-257.
29. Bello, F.; Page, A. F.; Pusch, A.; Hamm, J. M.; Donegan, J. F.; Hess, O., Combining E-near-Zero Behavior and Stopped Light Energy Bands for Ultra-Low Reflection and Reduced Dispersion of Slow Light. *Scientific Reports* **2017,** *7* (1), 8702.
30. Azzam, R. M. A.; Ugbo, E. E., Contours of Constant Pseudo-Brewster Angle in the Complex ∈ Plane and an Analytical Method for the Determination of Optical Constants. *Appl. Opt.* **1989,** *28* (24), 5222-5228.
31. Oughstun, K. E., Modified Brewster and Pseudo-Brewster Angles at the Interface between Isotropic Lossy Media. *J. Opt. Soc. Am. A* **2020,** *37* (9), 1505-1511.
32. Takayama, O.; Lavrinenko, A. V., Optics with Hyperbolic Materials [Invited]. *J. Opt. Soc. Am. B* **2019,** *36* (8), F38-F48.
33. Newman, W. D.; Cortes, C. L.; Atkinson, J.; Pramanik, S.; DeCorby, R. G.; Jacob, Z., Ferrell–Berreman Modes in Plasmonic Epsilon-near-Zero Media. *ACS Photonics* **2015,** *2* (1), 2-7.
34. Junfeng, L.; Xiang, D.; Xinglong, Y.; Dongsheng, W., Data Analysis of Surface Plasmon Resonance Biosensor Based on Phase Detection. *Sensors and Actuators B: Chemical* **2005,** *108* (1), 778-783.
35. Wu, F.; Thomas, P. A.; Kravets, V. G.; Arola, H. O.; Soikkeli, M.; Iljin, K.; Kim, G.; Kim, M.; Shin, H. S.; Andreeva, D. V.; Neumann, C.; Küllmer, M.; Turchanin, A.; De Fazio, D.; Balci, O.; Babenko, V.; Luo, B.; Goykhman, I.; Hofmann, S.; Ferrari, A. C.; Novoselov, K. S.; Grigorenko, A. N., Layered Material Platform for Surface Plasmon Resonance Biosensing. *Scientific Reports* **2019,** *9* (1), 20286.

36. Rhodes, C.; Cerruti, M.; Efremenko, A.; Losego, M.; Aspnes, D. E.; Maria, J.-P.; Franzen, S., Dependence of Plasmon Polaritons on the Thickness of Indium Tin Oxide Thin Films. *Journal of Applied Physics* **2008,** *103* (9), 093108.
37. Losego, M. D.; Efremenko, A. Y.; Rhodes, C. L.; Cerruti, M. G.; Franzen, S.; Maria, J.-P., Conductive Oxide Thin Films: Model Systems for Understanding and Controlling Surface Plasmon Resonance. *Journal of Applied Physics* **2009,** *106* (2), 024903.
38. Hilfiker, J. N.; Singh, N.; Tiwald, T.; Convey, D.; Smith, S. M.; Baker, J. H.; Tompkins, H. G., Survey of Methods to Characterize Thin Absorbing Films with Spectroscopic Ellipsometry. *Thin Solid Films* **2008,** *516* (22), 7979-7989.
39. Pluchery, O.; Vayron, R.; Van, K.-M., Laboratory Experiments for Exploring the Surface Plasmon Resonance. *European Journal of Physics* **2011,** *32* (2), 585-599.
40. Caligiuri, V.; Palei, M.; Biffi, G.; Artyukhin, S.; Krahne, R., A Semi-Classical View on Epsilon-near-Zero Resonant Tunneling Modes in Metal/Insulator/Metal Nanocavities. *Nano Letters* **2019,** *19* (5), 3151-3160.
41. Maier, S. A., Surface Plasmon Polaritons at Metal / Insulator Interfaces. In *Plasmonics: Fundamentals and Applications*, Maier, S. A., Ed. Springer US: New York, NY, 2007; pp 21-37.
42. Kuncova-Kallio, J.; Jokinen, A.; Sadowski, J. W.; Granqvist, N. In *Characterization of Nanolaminate Thickness Using Multi-Parametric Surface Plasmon Resonance*, 2013 International Conference on Manipulation, Manufacturing and Measurement on the Nanoscale, 26-30 Aug. 2013; 2013; pp 259-263.
43. Khani, S.; Hayati, M., An Ultra-High Sensitive Plasmonic Refractive Index Sensor Using an Elliptical Resonator and Mim Waveguide. *Superlattices and Microstructures* **2021,** *156*, 106970.
44. de Ceglia, D.; Scalora, M.; Vincenti, M. A.; Campione, S.; Kelley, K.; Runnerstrom, E. L.; Maria, J.-P.; Keeler, G. A.; Luk, T. S., Viscoelastic Optical Nonlocality of Low-Loss Epsilon-near-Zero Nanofilms. *Scientific Reports* **2018,** *8* (1), 9335.

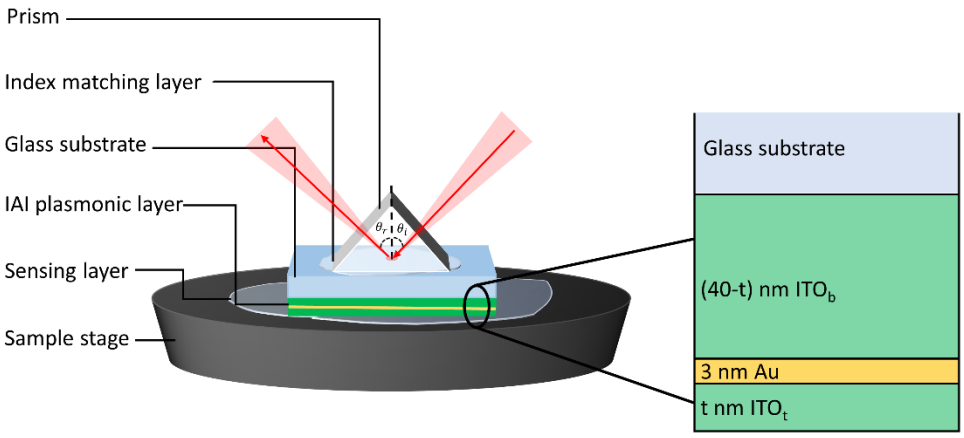

For Table of Contents Only